Three-Dimensional Electronic Microfliers With Designs Inspired by Wind-Dispersed Seeds

John Rogers (jrogers@northwestern.edu)
Northwestern University https://orcid.org/0000-0002-2980-3961

Bong Hoon Kim
Soongsil University

Kan Li
University of Cambridge

Jin-Tae Kim
Northwestern University

Yoonseok Park
Northwestern University https://orcid.org/0000-0002-1702-0986

Hokyung Jang
University of Wisconsin Madison https://orcid.org/0000-0002-7797-9881

Xueju Wang
University of Connecticut

Zhaoqian Xie
Dalian University of Technology https://orcid.org/0000-0003-1320-817X

Sang Won
Sungkyunkwan University

Woo Jin Jang
University of Illinois

Kun Hyuk Lee
Northwestern University

Ted Chung
Northwestern University https://orcid.org/0000-0002-0212-1071

Yei Hwan Jung
Hanyang University

Seung Yun Heo
Northwestern University

Yechan Lee
Korea Advanced Institute of Science and Technology

Juyun Kim
University of Illinois

Tengfei Cai

University of Illinois
Yeonha Kim
University of Illinois
Poom Prasopsukh
University of Illinois
YongJoon Yu
NeuroLux Corporation https://orcid.org/0000-0003-0142-1600
Xinge Yu
City University of Hong Kong https://orcid.org/0000-0003-0522-1171
Haiwen Luan
Northwestern University
Honglie Song
Tsinghua University
Feng Zhu
Wuhan University of Technology
Ying Zhao
Tongji University
Lin Chen
Xi'an Jiaotong University
Seung Ho Han
Korea Electronics Technology Institute
Jiwoong Kim
Soongsil University
Soong Ju Oh
Korea University
Heon Lee
Korea University
Chi Hwan Lee
Purdue University West Lafayette https://orcid.org/0000-0002-4868-7054
Yonggang Huang
Northwestern University https://orcid.org/0000-0002-0483-8359
Leonardo Chamorro
University of Illinois at Urbana Champaign https://orcid.org/0000-0002-5199-424X
Yihui Zhang
Tsinghua University https://orcid.org/0000-0003-0885-2067

Physical Sciences - Article

Keywords: Bio-inspired design, three-dimensional fabrication, fluid dynamics, aerodynamics, wireless electronics, air pollution sensors

Posted Date: January 14th, 2021

DOI: https://doi.org/10.21203/rs.3.rs-142068/v1

Version of Record: A version of this preprint was published at Nature on September 22nd, 2021. See the published version at https://doi.org/10.1038/s41586-021-03847-y.

Three-Dimensional Electronic Microfliers With Designs Inspired by Wind-Dispersed Seeds

Bong Hoon Kim[1†], Kan Li[2†], Jin-Tae Kim[3†], Yoonseok Park[3†], Hokyung Jang[4], Xueju Wang[5], Zhaoqian Xie[6], Sang Min Won[7], Woo Jin Jang[8], Kun Hyuk Lee[3], Ted S. Chung[3], Yei Hwan Jung[9], Seung Yun Heo[3], Yechan Lee[10], Juyun Kim[8], Tengfei Cai[11], Yeonha Kim[8], Poom Prasopsukh[11], Yongjoon Yu[3], Xinge Yu[12], Haiwen Luan[3,13], Honglie Song[14], Feng Zhu[15], Ying Zhao[16], Lin Chen[17], Seung Ho Han[18], Jiwoong Kim[1], Soong Ju Oh[19], Heon Lee[19], Chi Hwan Lee[20], Yonggang Huang[13*], Leonardo P. Chamorro[11*], Yihui Zhang[14*], John A. Rogers[3,21*]

[1] Department of Organic Materials and Fiber Engineering
Department of Smart Wearable Engineering
Soongsil University, Seoul 06978, Republic of Korea

[2] Department of Engineering
University of Cambridge, Cambridge CB2 1PZ, United Kingdom

[3] Querrey Simpson Institute for Bioelectronics
Northwestern University, Evanston, Illinois 60208, United States

[4] Department of Electrical and Computer Engineering
University of Wisconsin Madison, Madison, Wisconsin 53706, United States

[5] Department of Materials Science and Engineering, Institute of Materials Science
University of Connecticut, Storrs, Connecticut 06269, United States

[6] State Key Laboratory of Structural Analysis for Industrial Equipment
Department of Engineering Mechanics
Dalian University of Technology, Dalian 116024, People's Republic of China
Ningbo Institute of Dalian University of Technology, Ningbo, 315016, People's Republic of China

[7] Department of Electrical and Computer Engineering
Sungkyunkwan University, Suwon 16419, Republic of Korea

[8] Department of Chemical and Biomolecular Engineering
University of Illinois, Urbana, Illinois 61801, United States

[9]Department of Electronic Engineering
Hanyang University, Seoul 04763, Republic of Korea

[10] Department of Chemical and Biomolecular Engineering

Korea Advanced Institute of Science and Technology, Daejeon 34141, Republic of Korea

[11] Department of Mechanical Science and Engineering
University of Illinois, Urbana, Illinois 61801, United States

[12] Department of Biomedical Engineering
City University of Hong Kong, Hong Kong 999077, China

[13] Departments of Civil and Environmental Engineering, Mechanical Engineering, and Materials Science and Engineering
Northwestern University, Evanston, Illinois 60208, United States

[14] Applied Mechanics Laboratory, Department of Engineering Mechanics
Center for Flexible Electronics Technology
Tsinghua University, Beijing 100084, People's Republic of China

[15] School of Logistics Engineering
Wuhan University of Technology, Wuhan 430063, People's Republic of China

[16] School of Aerospace Engineering and Applied Mechanics
Tongji University, 200092 Shanghai, People's Republic of China

[17] State Key Laboratory for Mechanical Behavior of Meterials,
School of Material Science and Engineering,
Xi'an Jiaotong University, Xi'an 710000, People's Republic of China

[18] Electronic Convergence Materials and Device Research Center
Korea Electronics Technology Institute, Seongnam 13509, Republic of Korea

[19] Department of Materials Science and Engineering
Korea University, Seoul 02841, Republic of Korea

[20] Weldon School of Biomedical Engineering
School of Mechanical Engineering
School of Materials Engineering
Purdue University, West Lafayette, Indiana 47907, United States

[21] Department of Materials Science and Engineering, Biomedical Engineering, Neurological Surgery, Chemistry, Mechanical Engineering, Electrical Engineering and Computer Science
Northwestern University, Evanston, Illinois 60208, United States

E-mail: y-huang@northwestern.edu; lpchamo@illinois.edu; yihuizhang@tsinghua.edu.cn; jrogers@northwestern.edu

Keywords: Bio-inspired design, three-dimensional fabrication, fluid dynamics, aerodynamics, wireless electronics, air pollution sensors

Large, distributed collections of miniaturized, wireless electronic devices may form the basis of future systems for environmental monitoring, population surveillance, disease management and other applications that demand coverage over expansive spatial scales. In this paper, we show that wind-dispersed seeds can serve as the bio-inspiration for unusual aerial schemes to distribute components for such networks via controlled, unpowered flight across natural environments or city settings. Techniques in mechanically guided assembly of three-dimensional (3D) mesostructures provide access to miniature, 3D fliers optimized for such purposes, in processes that align with the most sophisticated production techniques for electronic, optoelectronic, microfluidic and microelectromechanical technologies. We demonstrate a range of 3D macro-, meso- and microscale fliers produced in this manner, including those that incorporate active electronic payloads. Analytical, computational and experimental studies of the aerodynamics of high-performance structures of this type establish a set of fundamental considerations in bio-inspired design, with a focus on 3D fliers that exhibit controlled rotational kinematics and low terminal velocities. Battery-free, wireless devices for atmospheric measurements provide simple examples of a wide spectrum of applications of these unusual concepts.

Plants spread their seeds through a remarkable variety of passive strategies, each the result of sustained processes of natural selection. Botanists classify these strategies according to their vectors for dispersal, the main types of which are gravity, ballistic, wind, water, and animals. Among these, wind is one of the most powerful and widely applicable. The 3D shapes of seeds optimized to exploit air flow in such contexts can support stable dynamics in controlled free-fall and/or facilitate transport over distances of up to hundreds of kilometers[1-3]. Although certain interactions between airborne seeds and the ambient air are well known, few research studies quantitatively define the essential

aerodynamics and none considers the potential relevance in microsystems technologies [4-6]. Just as plants use seeds and passive mechanisms for dispersal of genetic material to propagate the species, interesting opportunities might follow from use of similar approaches to distribute miniature electronic sensors, wireless communication nodes, energy harvesting components and/or various internet-of-things (IoT) technologies as monitors to track environmental processes, as aids to guide remediation efforts or as components to support distributed surveillance. This paper introduces the foundational engineering science for practical realization of these ideas[7-11].

Wind-dispersed seeds adopt geometries that are shaped by forces of evolution to maximize dynamic stability and/or transport distance during passive free-fall. The character of motions induced by air flow defines three broad categories of seeds: (i) gliders such as those of the box elder (*Acer negundo*) and the big-leaf maple (*Acer macrophyllum*), (ii) parachuters such as those of the evergreen ash (*Fraxinus uhdei*) and the tipu tree (*Tipuana tipu*) and (iii) flutterers/spinners such as those of the empress tree (*Paulownia tomentosa*), the tree of heaven (*Ailanthus altissima*) and the jacaranda (*Facaranda mimosifolia*) (Fig. 1a). These designs serve as inspiration for man-made passive flier structures built using approaches introduced here and engineered to optimize aerial dispersal of functional payloads, including a range of electronic, optoelectronic, microfluidic and microelectromechanical systems technologies. The overall sizes span the microscale (half widths of wings < 1 mm; microfliers), mesoscale (half widths ~ 1 mm; mesofliers), and macroscale (half widths > 1 mm; macrofliers) with the capacity to integrate material elements and devices with critical feature sizes that extend into the nanometer regime. Fig. 1b compares the dimensions and the geometries of a representative 3D microflier to those of various seeds with elaborate designs.

The fabrication scheme exploits controlled mechanical buckling to convert planar precursor structures formed with state-of-the-art planar processing and lithographic techniques into desired 3D layouts. Specifically, releasing the strain in a prestretched elastomer substrate generates compressive

forces on these precursors through a collection of bonding sites. The result affects geometrical transformation through a continuous sequence of in- and out-of-plane displacements and rotational motions (Figs. 1c~e). When implemented with shape memory polymers (SMPs; a mixture of epoxy monomer (E44; China Petrochemical Corporation) and curing agent (D230; Sigma-Aldrich)) and sacrificial thin layers (Mg ~ 50 nm) at the bonding sites, the resulting 3D objects can be released as free-standing passive fliers (Fig. 1f)[11]. The designs and choices of bonding sites define the overall 3D architectures; the magnitude of strain release determines the extent of three dimensionality, qualitatively defined by the ratio of the height of the structures to their lateral dimensions (small, 3D; large, 3D+), as in Fig. 1c. This scheme provides access to systems that behave in any of the three bio-inspired modalities mentioned previously, with flat and/or curved wings, solid and/or perforated structural elements, and various numbers of articulations. A simple identifying nomenclature includes (i) a number to indicate the number of wings, (ii) a letter to describe the shape of wings (R = ribbons, M = membranes, PM = porous membranes, and H = Hybrid, as a combination of ribbons and membranes), and (iii) a number to define the 3D aspect ratio (e.g., height divided by the width). Fig. 1d shows pictures of three 3D microfliers (widths~500 μm) placed on a fingertip. Fig. 1e highlights a 10 x 10 array of micro-, and mesofliers in various sizes (widths = 0.5~2 mm; Fig. S1) and geometries, formed via a single assembly process on a common substrate. Mass quantities of fliers can be formed at high throughput, as illustrated in Fig. 1f.

The terminal velocity (v_T) associated with free-fall in still air serves as a simple metric to compare the aerodynamics of these fliers to seeds and other objects in nature. As described in the following, microfliers can exhibit values of v_T that are 10 to 15 times small than other objects with similar sizes (~1 mm) and weights (~ 10 mg), including brown rice, sesame seeds, and snow (Fig. 1g)[12]. 3D microfliers with features (diameter ~ 1 mm, mass 12.2 mg, type [3, M, 0.4]) inspired by those of tristellateia seeds (diameter ~ 19.8 mm, mass 18.2 mg, density ~ 0.11 mg/mm^3; Fig. S2)

exhibit v_T ~28 cm/s, which is a factor of 3 smaller than that of the seeds (v_T ~100 cm/s; Supplementary Video 1).

Computational Fluid Dynamics (CFD) simulations (see Methods and Fig. S3) and analytical approaches (Supplementary Notes 1-4) reveal the underlying aerodynamic mechanisms. The essence of the physics can be examined by decomposing complex flier configurations into discrete numbers of tilted blades, as in Fig. 2a. The drag coefficient, $C_D = W/(0.5\rho v_T^2 A)$, is a dimensionless parameter that characterizes the relationship between the terminal velocity (v_T) and the weight (W), where ρ is the density of air and A is the area of the 2D membrane of the flier, excluding the area of perforations (i.e., voids). Fig. 2b summarizes values of C_D computed by CFD at different Reynolds numbers (Re), where $\mathrm{Re} = 2r\rho v_T/\mu$, μ is the dynamic viscosity of air and $2r$ is the diameter of the flier. The results can be described empirically as $C_\mathrm{D} \approx G_0 + G_1/\mathrm{Re}$, where the first ($G_0$) and second ($G_1/\mathrm{Re}$) terms correspond to behaviors where inertial and viscous effects dominate, at high and low Re, respectively. The terminal velocity v_T can be then expressed as

$$v_T = -\frac{\mu G_1}{4r\rho G_0} + \sqrt{\left(\frac{\mu G_1}{4r\rho G_0}\right)^2 + \frac{2W}{\rho A G_0}} \quad (1)$$

where G_0 and G_1 depend on critical geometric parameters of the fliers, such as the areal fill factor ($\eta = A_0/\pi r^2$, where A_0 is the void-free membrane area), porosity ($p = A_{void}/A_0$, where A_{void} is the total area of voids) and the tilt angle of the blades (β) in the rotational direction. In particular, for macrofliers, Eq. (1) becomes

$$v_T \approx \sqrt{\frac{2W}{\rho A G_0}}; \quad (2)$$

while for meso- and micro- fliers, v_T

$$v_T \approx \frac{4rW}{\mu A G_1}, \quad (3)$$

consistent with CFD simulations (Fig. S4). As might be expected, the behaviors of microfliers and macrofliers depend mainly on G_0 and G_1, respectively; both parameters are important for mesofliers.

The v_T of microfliers and macrofliers depend mainly on μ and ρ, respectively (Fig. S5). The results of CFD (Fig. 2c) show that the flow fields associated with microfliers ($2r\sim0.4$mm, Re$\sim$3; near the Stokes regime) and mesofliers ($2r\sim2$mm, Re$\sim$40) are laminar, while those of macrofliers ($2r\sim40$mm, Re$\sim$3000) are turbulent.

Mesofliers with different 3D configurations exhibit a common dependence of v_T on fill factor (Fig. 2d, Fig. S6, and Supplementary Note 1), $v_T = \frac{4}{\mu G_1}\left(\rho_m t_m g r\sqrt{\eta} + \frac{W_{\text{load}}}{\pi r\sqrt{\eta}}\right)$, as obtained from Eq (3), which is dominated by the viscous term, where W_{load} is the weight of the payload, ρ_m is the density of the structural material, t_m is the thickness, and g is the gravity acceleration. This equation indicates the existence of an optimal fill factor, i.e., $\eta_{\text{optimal}} = W_{load}/\pi r^2 \rho_m t_m g$, that minimizes the terminal velocity for a given W_{load}.

Parachute type seeds incorporate bundles of filaments with high effective porosity $p \approx 0.9$. Such configurations can be mimicked to a certain degree by introducing arrays of perforating holes (i.e., voids) in the structural components of the fliers. The result enhances C_D and reduces v_T [4], with different effects on G_0 and G_1 (Fig. 2b, Figs. S7-S9, and Supplementary Note 2). For example, porosity (e.g., $p = 0.25$) has a smaller effect on v_T (by ~ 10%) for macrofliers than for microfliers (by ~ 20%), as shown in Fig. S10. By contrast, the effects of curvature and tilt angle (β) in the blades of macrofliers (Fig. S11, S12) are more significant than those of microfliers (Supplementary Note 3).

Factors related to the properties of air, i.e., altitude, humidity, temperature or molecular makeup, influence the behaviors mainly through ρ and μ. For example, increasing the altitude from 0 to 80 km decreases ρ by a factor of 5, but the value of μ decreases by less than 25% (Fig. S13). Therefore, as shown by the CFD simulation results in Fig. 2e, mesofliers exhibit small v_T even at high altitudes (e.g., $\sim$1.36 m/s at 80 km altitude for $2r\sim2$ mm). By comparison, macrofliers have large v_T at such altitudes (e.g., $>$ 100 m/s at 80 km altitude for $2r\sim40$ mm). In a similar way, the

temperature and molecular makeup of the air can lead to opposite effects for micro- and macrofliers (Figs. S14 and S15).

Rotational behaviors (e.g., rotational speed ω_T) that follow from the 3D configuration (characterized by β) can confer kinematic stability. Analytical modeling (Supplementary Note 2), validated by CFD (Fig. S16), shows that $\omega_T \propto v_T/r$. With $\beta = 0$, rotation does not occur (Fig. S17). Stability can be analyzed by considering the microflier as a rotating rigid body driven by forces associated with air flow and subjected to small perturbations to its angular speed ($\dot{\Lambda}_1 = \Lambda_0 \cdot 1\mathrm{s}^{-1}$ in direction 1) from an initial balanced state (Fig. 2f and Supplementary Note 4), where Λ_1 and Λ_2 denote the perturbation angles with respect to directions 1 and 2, respectively. Studies of three representative structures (i.e., a 2D precursor; a 3D mesoflier without rotation, i.e., $\beta = 0$, see Fig. S7; and a 3D mesoflier with rotation, all with the same size ($2r$~2 mm) and fill factor ($\eta \approx 0.35$)) reveal the essential effects. Fig. 2g shows the perturbed angles (Λ_1/Λ_0 and Λ_2/Λ_0) as a function of time (t) after perturbation. The 2D precursor structure does not return to the balanced state. The 3D microflier without rotation returns to the balanced state quickly, but the maximum perturbed angle ($\max\left(\frac{1}{\Lambda_0}\sqrt{\Lambda_1^2+\Lambda_2^2}\right) \sim 0.025$) is much larger than that of the 3D microflier with rotation ($\max\left(\frac{1}{\Lambda_0}\sqrt{\Lambda_1^2+\Lambda_2^2}\right) \sim 0.018$). A normalized stability factor, Γ, as defined by

$$\Gamma = \min\left[\mathrm{Real}\left(\left(1 \pm \frac{\omega_0}{\beta_0} i\right) \pm \sqrt{\left(1 \pm \frac{\omega_0}{\beta_0} i\right)^2 - \frac{4\gamma}{\beta_0^2}}\right)\right], \tag{4}$$

can characterize the stability, in which ω_0/β_0 and $4\gamma/\beta_0^2$ account for the influences of material parameters, geometrical parameters and air properties (Fig. 2h, Supplementary Note 4), as given by

$$\beta_0 = \frac{\pi}{8}\frac{\mu r^2}{\sqrt{\eta}} \cdot \mathrm{Re}\left(2G_0 + \frac{G_1}{\mathrm{Re}}\right)\frac{1}{I_1},\ \omega_0 = \frac{I_3 - I_2}{I_1}\omega_T,\ \gamma = \frac{Wd}{I_1}, \tag{5}$$

where $I_{1,2,3}$ are the moment of inertias with respect to directions 1, 2 and 3, and d is the distance between the center of gravity and the center of pressure. A large positive value of Γ suggests that the

structure can quickly recover to its balanced, stable state; a negative value of Γ indicates that the structure is unstable. Additionally, the overall maximum perturbed angle, i.e., $\max\left(\frac{1}{\Lambda_0}\sqrt{\Lambda_1^2+\Lambda_2^2}\right)$, decreases monotonically with ω_0/β_0 (Fig. S18), consistent with rotational improvements in stability. Substitution of Eq. (1) into $\omega_T \propto v_T/r$ suggests that reducing r increases ω_T. As a result, increasing d and/or decreasing r can improve the stability through increases in $4\gamma/\beta_0^2$ and ω_0/β_0.

Experimental studies and results of additional computational modeling reveal detailed features of these and related behaviors. One set of measurements involves 3D Particle Tracking Velocimetry (3D-PTV), with a focus on (i) characterizing the 3D trajectories, terminal velocities and the characteristics of aerodynamic stability, and (ii) capturing 3D patterns of flow in a still ambient environment (see Methods, Fig. S19a and Supplementary Video 2 and 3). Another set focuses on quantifying the wake produced by various fliers placed at the exit of a vertical wind tunnel by high-speed Particle Image Velocimetry (PIV) (see Methods, Fig. S19b, S20, S21 and Supplementary Video 4 and 5).

Data show that a 2D precursor for a 3D mesoflier [3,M,0.4], Y2, (diameter $2r = 2$ mm, weight $W = 119$ μN) exhibits nonrotating, random tumbling behaviors with v_T ($v_{T,2D} \approx 0.37$ m/s) larger than that of stable, rotational behaviors of a 3D mesoflier [3,M,0.4], Y, (Fig. 3a and Supplementary Video 2 and 3), v_T ($v_{T,3D} \approx 0.29$ m/s). Introducing porosity into the same structure, YP, promotes further reductions in v_T ($v_{T,3D\,porous} \approx 0.28$ m/s; $\eta = 0.26$; Fig. 3b). These results agree with theoretical predictions and simulations, as in Fig. 2c. Across this same set of samples, the 3D shapes reduce the standard deviation of v_T by ~40% due to the enhanced aerodynamic stability ($\sigma_{2D} \approx 0.06$ m/s, $\sigma_{3D} \approx 0.03$ m/s, $\sigma_{3D\,porous} \approx 0.02$ m/s), consistent with the measured trajectories (Fig. 3c). Specifically, the 3D mesofliers travel in a straight downward direction, while the 2D precursors exhibit abnormal, chaotic falling behaviors with a time-

dependent combination of fluttering and gliding[13-15]. These latter processes lead to large variations in v_T and in settling location.

The 3D wake structures measured with 3D-PTV highlight additional features. Two representative instants in time (Figs. 3d and Fig. S22) show flow separations, as highlighted by the blue isosurface (flow structures in the opposite direction of the fall) and momentum deficits noted by the red isosurface (flow structures in the direction of the fall). The wake for the 2D flier exhibits comparatively large flow structures against the motion, with small flow structures along the motion at this instant and at other times throughout the fall. The 3D mesoflier induces comparatively small and rotating flow structures oriented against the motion, with large following structures. Large flow structures against the fall in the 2D precursor indicate early flow separation, which promotes comparatively high pressure gradients and aerodynamic instabilities. Small structures in the direction of the fall indicate small momentum deficits and, consequently, low drag and correspondingly large v_T. The rotational dynamics of the 3D mesofliers minimize flow separation and induce large momentum deficits, resulting in stable and slow falling behaviors (Supplementary Video 6).

Complementary insights follow from high-speed PIV measurements of instantaneous velocity fields (Fig. S23), mean velocity fields (Fig. 3e), velocity profiles (Fig. 3f) and velocity fluctuation profiles (Fig. 3g and h). The 3D mesoflier (Fig. 3e and f, Fig. S23) produces a larger wake and higher vertical velocity fluctuations, $\sigma(u)$, than the 2D precursor (Fig. 3g). Notably, the fluctuations for the 2D case show asymmetrical distributions due to its planar geometry and nonrotating behavior (Fig. 3h), as additional sources of instability. Symmetry in velocity fluctuations and large momentum deficits are consistent with the enhanced aerodynamics of 3D mesofliers.

Like seeds, these 3D platforms can transport payloads with passive or active functionality. The fabrication scheme affords many possibilities in functional integration, spanning nearly all forms of planar microsystems and semiconductor technologies. Fig. 4a shows an exploded view illustration

of 3D mesofliers, i.e. [3, M, 0.4] and [3, H, 0.75], that support semiconductor devices based on silicon nanomembranes (Si NMs; thickness 200 nm) as the active material, i) n-channel Si NM metal oxide semiconductor field effect transistors (nMOSFETs; channel lengths/widths of 20/80 μm) with SiO_2 gate dielectrics (thickness ~ 50 nm) and metal electrodes for gate, source and drain (Cr/Au, thickness ~ 5/50 nm), and ii) Si NM diodes formed with similar materials, respectively. The 3D structures are similar to those featured in the CFD simulations (Figs. S24 ~ S28). Layers of polyimide on the bottom and the top enhance the structural integrity of the SMP and improve the rigidity of the overall device. They also place the Si NM near the neutral mechanical plane to minimize the potential for fracture during assembly and use[16,17]. The electrical properties of the devices are consistent with those expected for monocrystalline silicon devices formed in the usual way on planar wafer substrates (Fig. S29). Optical micrographs in Fig. 4b highlight the geometries of the 2D precursors and the locations of the bonding sites. Fig. 4c&d show pictures of a 3 x 3 array of 3D mesofliers [3, M, 0.4] with Si NM nMOSFETs and corresponding 3D surface profiles determined using a laser scanning confocal microscope (Keyence VK-X1000).

As a simple application example, these types of electronic 3D microfliers can be released into the atmosphere from aircraft to track relevant environmental characteristics from positions at high altitudes to the ground, in large-area, dispersed configurations, as a complement to conventional gravimetric and optical particle counting methods[18,19] performed at stationary, localized positions. Fliers for such purposes support wireless, miniaturized battery-free light dosimeters designed for operation in the ultraviolet-A (UVA) band of the solar spectrum, according to recently reported schemes[20]. A photodiode (PD) generates photocurrent with a magnitude proportional to the UVA intensity. This current continuously charges a supercapacitor (SC) as a continuous, accumulation mode of detection during and after free fall. The electronics include a system-on-a-chip (SoC) with near field communication (NFC) capabilities and an analog-to-digital converter (ADC; Specification)

with a general-purpose-input/output (GPIO). An external reader device activates the SoC to measure the voltage across the SC, retrieve the corresponding digital data and to discharge the SC, all in a single operation (Fig. 4e, Fig. S30, S31, and Table S1). The measured dose depends on atmospheric conditions, including the pollution levels across altitudes, solar activity and other factors. Fig. 4f demonstrates the quantitative effect of air-born particles (Fig. S32).

The aerodynamics of these 3D IoT macrofliers (Figs. 4g~i and Fig. S33 ~ S36) are consistent with preceding discussions of the physics. The wakes exhibit oscillating tip vortices in the vicinity of the wings and a secondary vortex behind the center (Fig. 4g and Supplementary Video 7). Mean streamwise velocity fields (Fig. 4h) are similar to those of mesofliers with similar designs. Figure 4i shows that across a range of centimeter scale dimensions, the normalized transverse velocity profiles exhibit self-similarity, allowing for efficient dimensional analysis and modeling; inferred drag coefficients are shown in Fig. S33c and d).

The bio-inspired ideas and engineering foundations for mesoscale 3D fliers introduced here establish a set of unusual capabilities in aerial dispersal of advanced device technologies. Although not explicitly studied in this research, the effects of wind, thermal air currents and fluctuating air flows represent important practical considerations that tend to increase in significance as the sizes and the masses of the fliers decrease. The low terminal velocities of flutterers/spinners are of interest partly because they maximize the time for engagement with these flows, to increase the net transport distance. Gliders and parachuters represent alternative platforms that can be realized using similar constituent materials, fabrication processes, experimental methods and computational techniques. Layouts that combine these various design strategies may offer enhanced levels of performance, beyond those observed in nature. In addition to payloads that support active semiconductor functionality, responsive materials structures that change in color, shape or radio frequency signature according to environmental cues may serve as simple, complementary options for remote monitoring.

For many applications of distributed sensors and electronic components, efficient methods for recovery and disposal must be carefully considered. One solution is in devices constructed from materials that naturally resorb into the environment via a chemical reaction and/or physical disintegration to benign end products[21-23]. In these and other cases, eco-resorbable piezoelectric actuators or alternative active mechanical components may enhance control over flight dynamics. Such possibilities represent promising directions for future work.

Methods

Three-Dimensional (3D) Micro-, Meso- and Macrofliers. Fabrication of 2D precursors in thin films of SMP (thickness ~ 5 μm) began with a mixture (a mass ratio of 7:3) of epoxy monomer (E44, molecular weight $\approx$ 450 g mol^{-1}, China Petrochemical Corporation) and curing agent (D230, poly(propylene glycol) bis(2-aminopropyl)ether, Sigma-Aldrich). Spin coating and thermally curing (100 °C, 3 h) this mixture onto a sacrificial layer of a water-soluble polymer (spin cast; poly(4-styrenesulfonic acid, 500 nm), PSA; Sigma-Aldrich) on a silicon wafer defined a thin film of SMP. Electron beam evaporation of gold (Au, thickness ~ 10/50 nm) followed by photolithography and wet etching formed a metal hard mask for patterned removal of exposed regions of the SMP by oxygen plasma reactive ion etching (O_2 RIE). Removing the Au and the underlying PSA facilitated the retrieval of the patterned SMP onto a water-soluble tape (polyvinyl alcohol, 3M Corporation). A multilayer of Ti/Mg/Ti/SiO_2 (thickness ~ 5/50/5/50 nm) deposited through a shadow mask by electron beam evaporation defined sites for chemical bonding, activated by exposure to ozone to create surface hydroxyl termination on the SiO_2. Transfer onto a pre-strained silicone elastomer substrate (Ecoflex, Smooth-On) led to strong covalent bonding only at these locations, with weak van der Waals adhesion forces at all other regions. Releasing the prestrain led to mechanical buckling and a corresponding 2D to 3D geometric transformation. Heating to 70 °C for 1 min in an oven followed by cooling to room temperature fixed the 3D shape via shape memory effects. Immersing the structure in water eliminated the Mg layer and released the structures as free-standing objects.

3D Electronic Mesofliers. Fabrication of the silicon (Si) nanomembranes (NM) nMOS transistors began by defining regions of phosphorus doping using spin-on-dopants (950 °C, 8 min) on a silicon on insulator (SOI, top silicon thickness ~ 200 nm, SOITEC, France) wafer for source and drain contacts. For Si NM diodes, the doping involved both phosphorus (1050 °C, 15 min) and boron (1100 °C, 30 min) to define p-n junctions. Removing the buried silicon dioxide (SiO_2) by wet etching released the top device silicon from the SOI wafer, and enabled transfer printing of the resulting Si NMs onto spin-cast films of polyimide (PI, thickness ~ 3 μm, HD microsystems INC) on a sacrificial layer of polymethylmethacrylate (PMMA, thickness ~ 100 nm, MicroChem INC) on a silicon wafer. Photolithography and reactive ion etching (RIE, Plasma Therm, Inc., USA) with sulfur hexafluoride gas (SF_6, 100 mTorr, 50 W, 40 sccm, 200 s) left the top silicon only in the active regions of the device. A thin layer of SiO_2 (thickness ~ 50 nm) formed by PECVD served as the gate dielectric for Si NM

nMOS transistors. A bilayer of Cr/Au (thickness ~ 5/100 nm) deposited by electron beam evaporation and patterned by photolithography served as electrodes and interconnects. Spin casting a thin layer of PI (thickness ~ 3 μm) and etching by RIE (O_2 gas, 150 mTorr, 100 W, 20 sccm) completed the formation of an ultra-thin active device layer composed of Si NM devices and metal interconnects. Dissolving the PMMA layer with acetone released the devices from the silicon wafer. Lastly, the Si NMs device layer encapsulated by a film of PI was transfer printed onto a thin film of SMP (thickness ~ 5 μm) using a PDMS stamp. Additional steps to create 3D electronic mesofliers from these 2D precursors followed those outlined above.

3D Internet of Things (IoT) Macrofliers. Fabricating the 2D precursors began with spin-coating films of SMP (thickness ~ 12 μm) onto thick Cu foils (thickness ~ 18 μm). A pattern of photoresist served as a mask for wet etching (CE-100 etchant, Transene) the copper foil to define a metal interconnect structure for the electronic components. After using a laser cutting process to pattern the film of SMP, mounting an NFC chip (Texas Instruments, RF430FRL152HCRGER), a collection of photodiodes (Advanced Photonix, PDB-CD160SM), a set of MOSFETs (Texas Instruments, CSD17381F4), super-capacitors (Seiko Instruments, CPH3225A) and capacitors (Murata Electronics North America / TDK, GRM033R60J225ME47D / C0603X7R1A103K030BA & C0603X5R1A104K030BC) at defined locations on the 2D precursor with conductive epoxy (Allied Electronics) yielded a digital sensing system. Additional steps to create 3D IoT macrofliers from these 2D precursors followed those outlined above.

Optical experiments with particulate matter (PM) pollution. The 3D IoT macroflier uses a millimeter-scale, wireless, and battery-free NFC platform with an electronic circuit for accumulation mode dosimetry in the UVA region of the solar spectrum, where the flux depends, in part, on airborne particulates. The photodiodes generate a photocurrent with a magnitude that correlates with the instantaneous exposure intensity. This current continuously charges the SC such that the accumulated charge, measured by the voltage, defines the exposure dose[20]. A dust generation chamber operated with incense sticks, smoke cakes, corn starch, and kitchen blenders served as a platform to investigate the influence of fine particulate pollution on the measured response (Fig. S30).

Experiments using 3D-Particle Tracking Velocimetry (3D-PTV). The studies involved two types of measurements, both performed using 3D-PTV in a customized channel (Fig. S19a): (1) 3D

trajectories of free-falling microfliers with 2D, 3D and 3D porous designs and (2) associated 3D induced flows. The upper part of the test chamber consisted of a 1.5m-long glass tube with an inner diameter of 0.01 m to (i) minimize anomalous behaviors such as tumbling and (ii) ensure steady-state behavior. The lower part included an acrylic glass enclosure with inner dimensions of $0.1 \times 0.1 \times 0.2$ m^3 (L × W × H), sufficiently large to minimize boundary effects. The investigation volume for the fliers had dimensions of $4 \times 4 \times 6$ cm^3, illuminated by an LED light source. The volume for visualizing 3D induced flows was $0.8 \times 0.8 \times 1.2$ cm^3, illuminated by a synchronized dual-cavity YLF laser with pulse energies of 50 mJ at repetition rates of 1 kHz (527-80-M, Terra). Oil droplets with diameters of $O(10^0)$ μm served as tracers. Recordings for 3D-PTV experiments used three digital cameras (2560 × 1600 pixels CMOS Phantom Miro 340 with 12 GB on-board memory and frame rates of 1,000 fps). A series of lenses (60 mm, focal ratio f/2.8, Nikon AF Micro-Nikkor) focused the images on the corresponding investigation volumes. Pre-processing, calibration, 3D reconstruction, tracking and post-processing exploited 3D-PTV codes described previously[24]. Tracking of the 3D reconstructed positions of fliers relied on the Hungarian algorithm linked by performing a three-frame gap closing to produce long trajectories. Associated temporal derivatives were filtered and estimated using fourth-order *B* splines. Additional details of the PTV system can be found elsewhere[25]. The free-falling experiments involved 10 repetitions for each sample to obtain statistically significant measurements of the stability and kinematics of the falling behaviors (Fig. 3c). Tracer particles were tracked in 3D and converted into inferred 3D Eulerian velocity vector fields that defined the 3D induced flows. Interpolating scattered Lagrangian flow particles at each frame based on the natural neighbor interpolation method yielded the 3D vector fields.

Experiments using High-Speed Particle Image Velocimetry (PIV) and a vertical wind tunnel. Two sets of experiments used high-speed PIV above a vertical wind tunnel (Fig. S19b) to define the wake dynamics of (1) fixed 2D precursors and 3D fliers exposed to flow velocities of $U \approx 0.4$ m/s, similar to those associated with terminal velocities in free fall and (2) working 3D fliers with five different diameters $d = 1$, 2, 3, 4 and 5 cm at $U \approx 1.2$, 2.4 and 3.6 m/s. For the latter, a 200 μm diameter and 4 cm long wire with an adhesive on the tip fixed the positions of the fliers (Fig. S20). The wire attached to a thin rectangular acrylic plate to minimize boundary effects on incoming flows. A customized vertical wind tunnel enabled measurements of wake dynamics around the fliers. A series of four fans (Mechatronics G8015X12B-AGR-EM) placed on the bottom of the tunnel produced air flows in the wind tunnel. A tunable power supply (Tekpower TP3005N Regulated DC Variable Power

Supply) calibrated by quantifying the background flow using PIV set the fan speed. The channel consisted of flow straighteners above the fans to smoothen the flows and an aluminum honeycomb grid above the contraction section. A 1/8" acrylic sheet machined by laser cutting defined the frame of the tunnel. A high-speed PIV system (TSI, Inc.) characterized the wake induced by meso- and macrofliers. Olive oil droplets served as tracers in the air. A 1 mm thick laser sheet produced by a synchronized dual-cavity YLF laser with pulse energies of 50 mJ at repetition rates of 100 Hz (527-80-M, Terra) illuminated the resulting flows. The field of view covered a 24.48 mm × 15.3 mm region above the fliers, with 950 image pairs collected for each case at a frequency of 100 Hz using a digital camera (2560× 1600 pixels CMOS Phantom Miro 340.) A recursive cross-correlation method (Insight 4G software, TSI Image) processed pairs of images. The first pass used a 64 × 64-pixel interrogation window. The final window had a size of 8 × 8-pixels with 50% overlap, resulting in a vector spacing $\Delta x = \Delta \mathrm{y} = 0.0765$ mm. For fifteen sets of PIV measurements on working fliers (three speed and five diameters), the field of view covered a 128 mm × 80 mm region with a vector spacing of $\Delta x = \Delta \mathrm{y} =$ 0.4 mm. Overall, more than 97% of the vectors were resolved in all measurements.

Finite Element Analysis. Three-dimensional FEA techniques quantitatively captured the mechanical deformations and the associated 3D configurations of the fliers in different scales, during processes of compressive buckling and bending under the flow of air. Eight-node shell elements were employed using commercial software (ABAQUS), with refined meshes to ensure computational accuracy. Linear elastic responses were used to model the SMP, with material parameters $E_{\mathrm{SMP}} = 2$ MPa and $\nu_{\mathrm{SMP}} = 0.3$. Parameters for the other materials were $E_{\mathrm{Cu}} = 110$ GPa, $\nu_{\mathrm{Cu}} = 0.3$ and $\sigma_{\mathrm{Y}} = 350$ MPa as a perfect elastic-plastic model for copper, $E_{\mathrm{Si}} = 190$ GPa and $\nu_{\mathrm{Si}} = 0.29$ as an elastic model for silicon.

Computational Fluid Dynamics. Three-dimensional CFD simulations defined the rotational falling behaviors of the fliers in a static state, using the 3D rotating machinery, laminar flow module in commercial software (COMSOL 5.2). First-order discretization (P1-P1) with a refined mesh ensured computational accuracy. Fliers with 3D configurations defined by FEA resided in the centered rotating region inside a large tube. The inflow velocities set at the bottom surface of the outer tube matched values equivalent to the terminal velocities of the fliers. The flier was set as the “rotating interior wall” in the rotating domain, as shown in Fig. S3, where the local velocity of air equals to the velocity of flier. The rotating speed of the rotating domain, which represents the rotating velocity of

the flier, corresponded to the value for which the torque of the air acting on the microflier equals zero. For a given terminal velocity, the force of air acting on the flier in the inflow direction matched its weight. The air was modeled as compressible flow, with properties at sea-level $\rho = 1.225\ \mathrm{kg/m^3}$ and $\mu = 17.89\ \mu\mathrm{Pa \cdot s}$. At large Reynolds numbers, the k-ω model captured the effects of turbulence. Two-dimensional CFD simulations captured the aerodynamic behaviors of the 2D airfoils in a similar manner.

Electromagnetic Simulations. The commercial software ANSYS HFSS was used to perform electromagnetic finite element analysis and to determine the inductance, Q factor for the 2D and 3D antennas. Lumped ports yielded the port impedance Z of the antennas. An adaptive mesh (tetrahedron elements) and a spherical radiation boundary (radius of 1000 mm) ensured computational accuracy. The inductance (L) and Q factor (Q) (shown in Fig. S28) were obtained from $L = \mathrm{Im}^4/(2\pi f)$ and $Q = |\mathrm{Im}^4/\mathrm{Re}^4|$, where Re^4, Im^4 and f represent the real and imaginary part of the Z and the frequency, respectively. The default material properties included in the HFSS material library were used in the simulation.

Acknowledgements

This work was supported by the Querrey Simpson Institute for Bioelectronics at Northwestern University. B.H.K. acknowledges the support from the National Research Foundation of Korea (NRF) grant funded by the Korea government (MSIT) (No.2020R1C1C1014980), Creative Materials Discovery Program through the National Research Foundation of Korea (NRF) funded by Ministry of Science and ICT (NRF-2018M3D1A1058972), and Korea Institute for Advancement of Technology (KIAT) grant funded by the Korea Government (MOTIE) (P0012770). Y.Z. acknowledges the support from the National Natural Science Foundation of China (Grant Nos. 11722217 and 12050004), the Institute for Guo Qiang, Tsinghua University (Grant No. 2019GQG1012), and the Tsinghua National Laboratory for Information Science and Technology. H.L. acknowledge the support from Nanomaterial Technology Development Program (NRF-2016M3A7B4905613) through the National Research Foundation of Korea (NRF) funded by the Ministry of Science, ICT and Future Planning. Z.X. acknowledges the support from the National Natural Science Foundation of China (Grant No. 12072057) and Fundamental Research Funds for the Central Universities (Grant No. DUT20RC(3)032).

Author Contributions

B.H.K., K.L., J.-T.K. and Y.P. contributed equally to this work. Y.H., L.P.C., Y.Z. and J.A.R. conceived the ideas and supervised the project. B.H.K., K.L., J.-T.K., Y.P., Y.H., L.P.C., Y.Z. and J.A.R. wrote the manuscript. H.J., X.W., S.M.W., W.J.J., K.H.L., Y.H.J., S.Y.H., Y.L., J.K., Y.K., Y.Y. and X.Y. performed microelectromechanical experiments. J.-T.K., T.C., and P.P. performed fluid dynamics experiments. Z.X., T.S.C., H.L., H.S., F.Z., Y.Z. and L.C. performed mechanical and electromagnetic simulation. S.H.H., J.K., S.J.O., H.L. and C.H.L. provided scientific and experimental advice. All authors commented on the manuscript.

Figure captions

Fig. 1 | 3D microfliers inspired by wind-dispersed seeds. a, Glider types: (1) the box elder (*Acer negundo*) and (2) the big-leaf maple (*Acer macrophyllum*); parachuter types: (3) the evergreen ash (*Fraxinus uhdei*) and (4) the tipu tree (*Tipuana tipu*); flutterers/spinner types: (5) the empress tree (*Paulownia tomentosa*), (6) the tree of heaven (*Ailanthus altissima*), and (7) the jacaranda (*Facaranda mimosifolia*). **b,** Schematic illustration that compares the sizes and morphologies of a *Diptocarpus alatus* seed, dandelion seed, and a representative 3D microflier. **c,** Mechanical simulation results for the geometrical transformation of ten different 2D precursors (grey; 2D, bottom row) into corresponding 3D structures with modest (green; 3D, middle row) and large (green; 3D+, top row) aspect ratios. The identifying terminology indicating beneath each case includes (i) a number to indicate the number of wings, (ii) a letter to describe the shape of wings (R = ribbons, M = membranes, PM = porous membranes, and H = Hybrid), and (iii) a number to define the 3D aspect ratio (e.g. height divided by the width). **d-f,** Photographs and optical micrographs of three different 3D microfliers [2,H,1.2], [3,H,0.6] (left), and [3,M,0.4], resting on the tip of a finger (right) (**d**), a 10 x 10 array (**e**), and a large collection of 3D microfliers (**f**). **g,** The terminal velocity of several small objects and a 3D microflier [3,M,0.4].

Fig. 2 | Theoretical analysis and numerical simulation of the aerodynamics associated with representative 3D micro-, meso- and macrofliers. a, Schematic diagram of a rotating 3D microflier [3,M,0.4] (top) and a simplified model (bottom) for purposes of theoretical analysis, with key variables indicated. **b,** Drag coefficient versus Reynolds number of various structures (i.e. 2D disk, and 3D microfliers [3,M,0.4] and [3,PM,0.4]). **c,** Terminal velocities of four different 3D microfliers X = [3,H,0.75], Y = [3,M,0.4], Z = [3,H,0.6], and W = [2,H,1.2] with various fill factors. **d,**

Instantaneous flow fields for 3D micro-, meso- and macrofliers. **e,** CFD prediction of the terminal velocity for 3D microfliers [3,M,0.4] at different size scales at different altitudes in the atmosphere, from sea level to 80 km. **f,** Schematic diagram of the stability analysis of a rotating 3D microflier [3,M,0.4] during free-fall. **g,** Behaviors of different 3D microfliers (a 2D precursor for a 3D microflier [3,M,0.4], and 3D microfliers [3,H,0.75] and [3,M,0.4]) with small perturbations of angular speed. **h,** Stability phase plot of 3D microfliers X = [3,H,0.75] and Y = [3,M,0.4] and a 2D precursor for a 3D microflier Y2 = [3,M,0.4].

Fig. 3 | Experimental measurements of the flow characteristics of representative 3D mesofliers. **a,** Optical images of Y2 = a 2D precursor for a 3D mesoflier [3,M,0.4] and a corresponding 3D mesoflier Y = [3,M,0.4] at various times during free fall. The former shows nonrotating and random tumbling behaviors; the latter exhibits strong rotational dynamics and a straight path trajectory. **b,** Mean terminal velocity and its standard deviation for Y2 = a 2D precursor for a 3D mesoflier [3,M,0.4] and 3D mesoflier Y = [3,M,0.4], and YP = a porous 3D mesoflier for [3,PM,0.4]. **c,** Falling trajectories upon release at an angle of 90^0, where 0^0 corresponds to the flat side parallel to the ground. Y2 = a 2D precursor for a 3D mesoflier [3,M,0.4] and 3D mesoflier Y = [3,M,0.4]. **d,** Instantaneous 3D flow velocity fields induced by a free-falling 2D precursor for a 3D mesoflier [3,M,0.4] (left) and a 3D mesoflier [3,M,0.4] (right) determined via 3D-PTV. Red and blue iso-surfaces indicate iso-values of 15 and -5 mm/s, respectively. The color denotes correlated CFD results of the in-plane 2D vertical velocity along the center plane of the flier. PIV measurements of instantaneous flow fields induced by a physically constrained a 2D precursor for a 3D mesoflier [3,M,0.4] and a 3D mesoflier [3,M,0.4] in a wind tunnel. **e,** Mean velocity fields of a 2D precursor for a 3D mesoflier [3,M,0.4] (left) and a 3D mesoflier [3,M,0.4] (right) in these conditions, with a wind velocity $U \approx 0.4$ m/s. **f, g,** Velocity profiles (**f**) and vertical velocity fluctuation profiles (**g**) at $x = 4$ mm downstream. **h,** Vertical velocity fluctuation $\sigma(u)$ for a 2D precursor for a 3D mesoflier [3,M,0.4] (left) and a 3D mesoflier [3,M,0.4] (right).

Fig. 4 | 3D electronic mesofliers and IoT macrofliers. **a,b,** Schematic illustration (**a**) and optical micrographs (**b**) of 2D precursors for 3D electronic mesofliers [3,M,0.4] and [3,H,0.75] with silicon nanomembrane (NM) nMOS transistors and diodes as payloads. **c,** Photograph of a 3 x 3 array of 3D electronic mesofliers [3, M, 0.4] with these payloads. **d,** 3D surface profile of a 3D mesoflier [3,M,0.4]. **e,** Mechanical simulation results and photograph of a 3D IoT macroflier with a circuit to

measure fine dust pollution through the light dosimetry method. **f,** Energy stored on the SC as a function of exposure time in the presence of 3 types of fine dust. High-speed PIV flow measurements for 3D IoT macrofliers (d=2 cm) with various diameters and air velocities. **g,** Instantaneous velocity field. **h,** Mean velocity field u/U. **i,** Normalized spanwise velocity profiles at 1.2 diameter downstream for 3D IoT macrofliers with diameters between 1 and 5 cm.

References

1 Nathan, R. *et al.* Mechanisms of long-distance dispersal of seeds by wind. *Nature* **418**, 409-413 (2002).

2 Nathan, R. Long-distance dispersal of plants. *Science* **313**, 786-788 (2006).

3 Seale, M. & Nakayama, N. From passive to informed: mechanical mechanisms of seed dispersal. *New Phytol.* **225**, 653-658 (2020).

4 Cummins, C. *et al.* A separated vortex ring underlies the flight of the dandelion. *Nature* **562**, 414-418 (2018).

5 Rabault, J., Fauli, R. A. & Carlson, A. Curving to fly: Synthetic adaptation unveils optimal flight performance of whirling fruits. *Phys. Rev. Lett.* **122**, 024501 (2019).

6 Fauli, R. A., Rabault, J. & Carlson, A. Effect of wing fold angles on the terminal descent velocity of double-winged autorotating seeds, fruits, and other diaspores. *Phys. Rev. E* **100**, 013108 (2019).

7 Xu, S. *et al.* Assembly of micro/nanomaterials into complex, three-dimensional architectures by compressive buckling. *Science* **347**, 154-159 (2015).

8 Zhang, Y. *et al.* A mechanically driven form of Kirigami as a route to 3D mesostructures in micro/nanomembranes. *P. Natl. Acad. Sci.* **112**, 11757-11764 (2015).

9 Zhang, Y. *et al.* Printing, folding and assembly methods for forming 3D mesostructures in advanced materials. *Nat. Rev. Mat.* **2**, 1-17 (2017).

10 Pang, W. *et al.* Electro-mechanically controlled assembly of reconfigurable 3D mesostructures and electronic devices based on dielectric elastomer platforms. *Natl. Sci. Rev.* **7**, 342-354 (2020).

11 Wang, X. *et al.* Freestanding 3D Mesostructures, Functional Devices, and Shape‐Programmable Systems Based on Mechanically Induced Assembly with Shape Memory Polymers. *Adv. Mater.* **31**, 1805615 (2019).

12 Zhang, L., Wang, X., Moran, M. & Feng, J. Review and uncertainty assessment of size-resolved scavenging coefficient formulations for below-cloud snow scavenging of atmospheric aerosols. *Atmos. Chem. Phys.* **13** (2013).

13 Belmonte, A., Eisenberg, H. & Moses, E. From flutter to tumble: inertial drag and Froude similarity in falling paper. *Phys. Rev. Lett.* **81**, 345 (1998).

14 Zhong, H. *et al.* Experimental investigation of freely falling thin disks. Part 1. The flow structures and Reynolds number effects on the zigzag motion. *J. Fluid Mech.* **716**, 228 (2013).

15 Kim, J.-T., Jin, Y., Shen, S., Dash, A. & Chamorro, L. P. Free fall of homogeneous and heterogeneous cones. *Phys. Rev. Fluids* **5**, 093801 (2020).

16 Kim, B. H. *et al.* Three-dimensional silicon electronic systems fabricated by compressive buckling process. *ACS nano* **12**, 4164-4171 (2018).

17 Won, S. M. *et al.* Multimodal Sensing with a Three-Dimensional Piezoresistive Structure. *ACS nano* **13**, 10972-10979 (2019).

18 Binnig, J., Meyer, J. & Kasper, G. Calibration of an optical particle counter to provide PM2. 5 mass for well-defined particle materials. *J. Aerosol Sci.* **38**, 325-332 (2007).

19 Shao, W., Zhang, H. & Zhou, H. Fine particle sensor based on multi-angle light scattering and data fusion. *Sensors* **17**, 1033 (2017).

20 Heo, S. Y. *et al.* Wireless, battery-free, flexible, miniaturized dosimeters monitor exposure to solar

radiation and to light for phototherapy. *Sci. Transl. Med.* **10**, eaau1643 (2018).
21 Hwang, S.-W. *et al.* A physically transient form of silicon electronics. *Science* **337**, 1640-1644 (2012).
22 Kang, S.-K., Koo, J., Lee, Y. K. & Rogers, J. A. Advanced materials and devices for bioresorbable electronics. *Accounts Chem. Res.* **51**, 988-998 (2018).
23 Lee, G., Choi, Y. S., Yoon, H.-J. & Rogers, J. A. Advances in Physicochemically Stimuli-Responsive Materials for On-Demand Transient Electronic Systems. *Matter* **3**, 1031-1052 (2020).
24 Kim, J.-T., Nam, J., Shen, S., Lee, C. & Chamorro, L. P. On the dynamics of air bubbles in Rayleigh-Benard convection. *J. Fluid Mech.* **891** (2020).
25 Kim, J.-T. & Chamorro, L. P. Lagrangian description of the unsteady flow induced by a single pulse of a jellyfish. *Phys. Rev. Fluids* **4**, 064605 (2019).

Figures

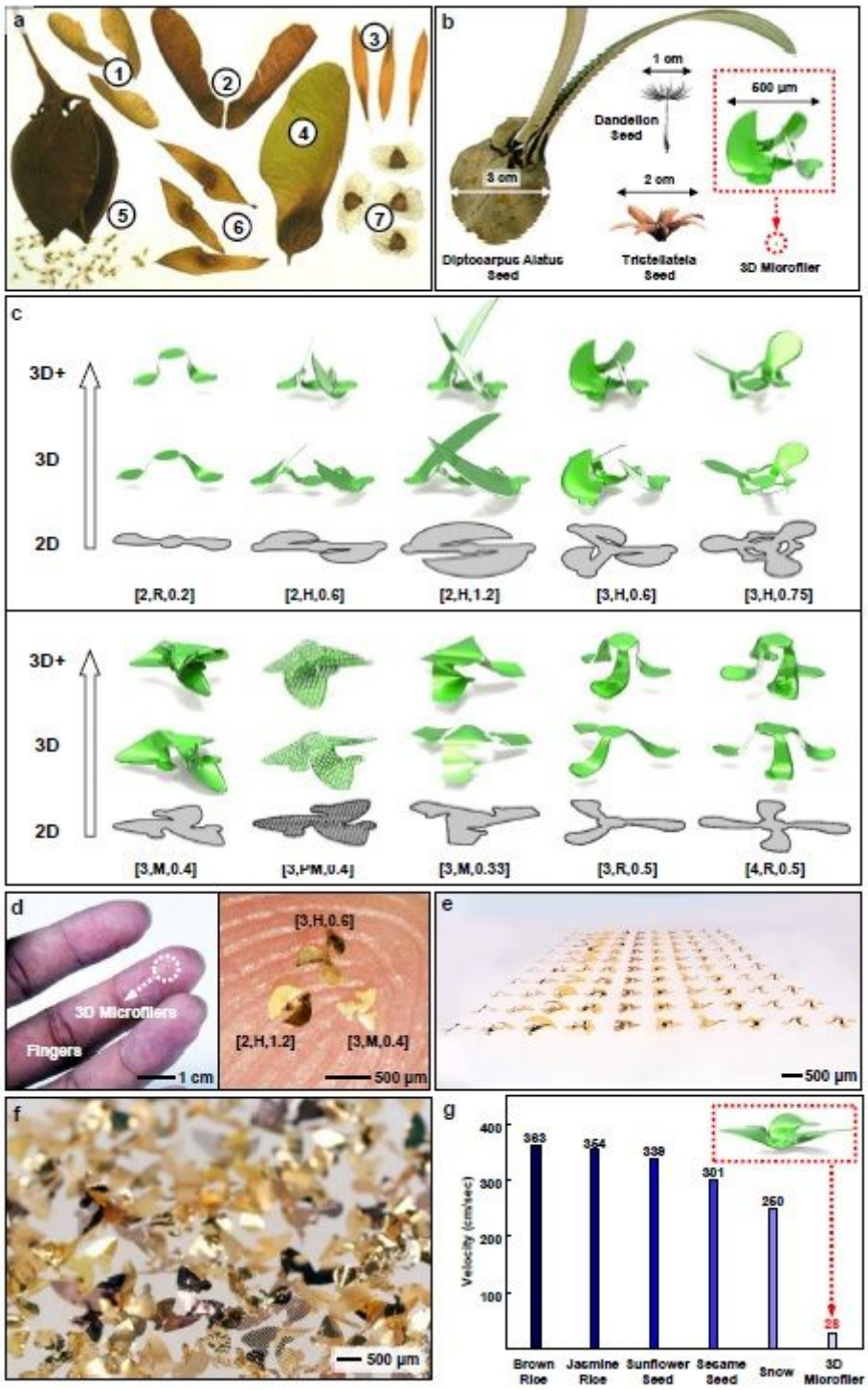

Figure 1

3D microfliers inspired by wind-dispersed seeds. a, Glider types: (1) the box elder (Acer negundo) and (2) the big-leaf maple (Acer macrophyllum); parachuter types: (3) the evergreen ash (Fraxinus uhdei) and (4) the tipu tree (Tipuana tipu); flutterers/spinner types: (5) the empress tree (Paulownia tomentosa), (6) the

tree of heaven (Ailanthus altissima), and (7) the jacaranda (Facaranda mimosifolia). b, Schematic illustration that compares the sizes and morphologies of a Diptocarpus alatus seed, dandelion seed, and a representative 3D microflier. c, Mechanical simulation results for the geometrical transformation of ten different 2D precursors (grey; 2D, bottom row) into corresponding 3D structures with modest (green; 3D, middle row) and large (green; 3D+, top row) aspect ratios. The identifying terminology indicating beneath each case includes (i) a number to indicate the number of wings, (ii) a letter to describe the shape of wings (R = ribbons, M = membranes, PM = porous membranes, and H = Hybrid), and (iii) a number to define the 3D aspect ratio (e.g. height divided by the width). d-f, Photographs and optical micrographs of three different 3D microfliers [2,H,1.2], [3,H,0.6] (left), and [3,M,0.4], resting on the tip of a finger (right) (d), a 10 x 10 array (e), and a large collection of 3D microfliers (f). g, The terminal velocity of several small objects and a 3D microflier [3,M,0.4].

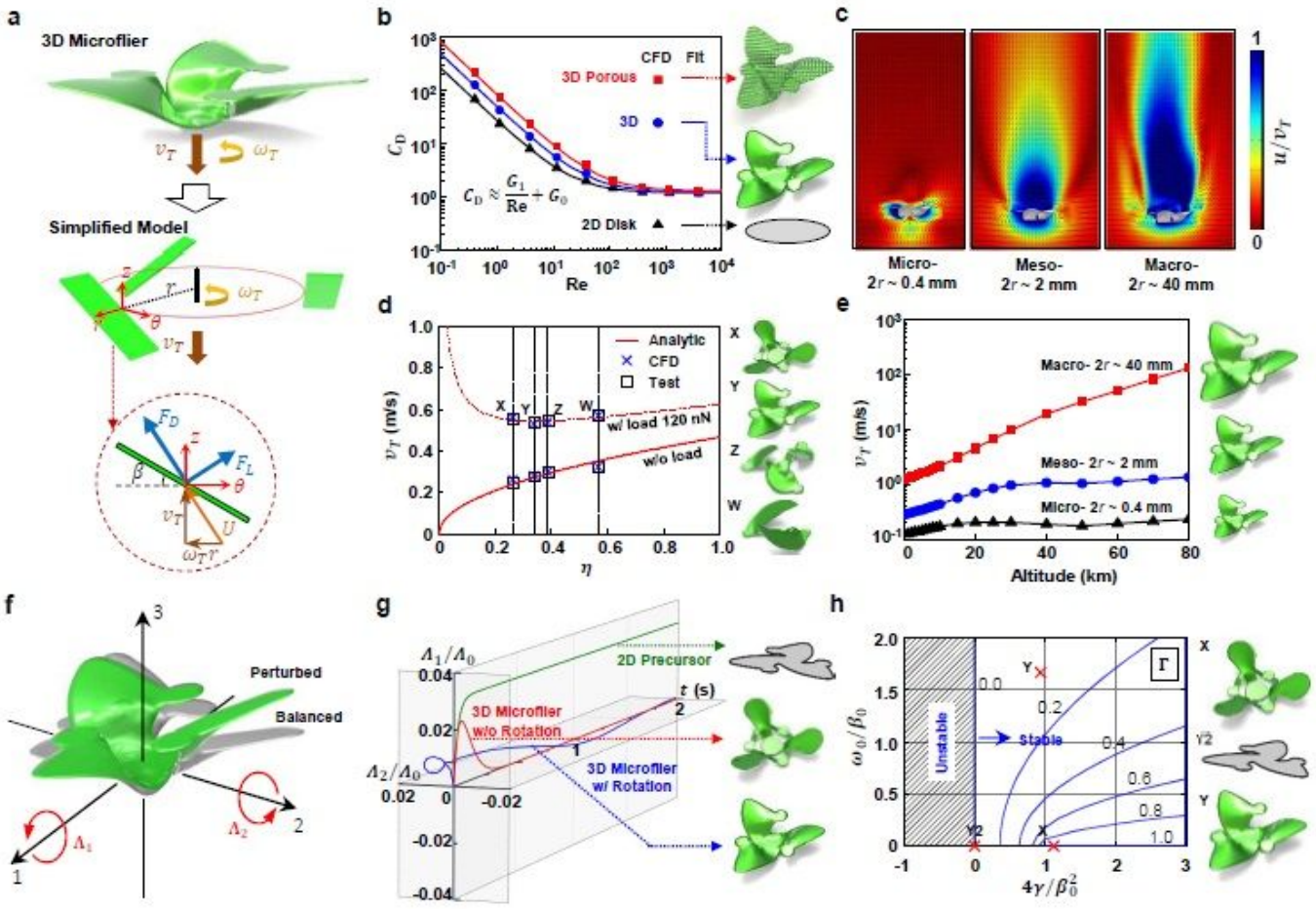

Figure 2

Theoretical analysis and numerical simulation of the aerodynamics associated with representative 3D micro-, meso- and macrofliers. a, Schematic diagram of a rotating 3D microflier [3,M,0.4] (top) and a simplified model (bottom) for purposes of theoretical analysis, with key variables indicated. b, Drag coefficient versus Reynolds number of various structures (i.e. 2D disk, and 3D microfliers [3,M,0.4] and

[3,PM,0.4]). c, Terminal velocities of four different 3D microfliers X = [3,H,0.75], Y = [3,M,0.4], Z = [3,H,0.6], and W = [2,H,1.2] with various fill factors. d, Instantaneous flow fields for 3D micro-, meso- and macrofliers. e, CFD prediction of the terminal velocity for 3D microfliers [3,M,0.4] at different size scales at different altitudes in the atmosphere, from sea level to 80 km. f, Schematic diagram of the stability analysis of a rotating 3D microflier [3,M,0.4] during free-fall. g, Behaviors of different 3D microfliers (a 2D precursor for a 3D microflier [3,M,0.4], and 3D microfliers [3,H,0.75] and [3,M,0.4]) with small perturbations of angular speed. h, Stability phase plot of 3D microfliers X = [3,H,0.75] and Y = [3,M,0.4] and a 2D precursor for a 3D microflier Y2 = [3,M,0.4].

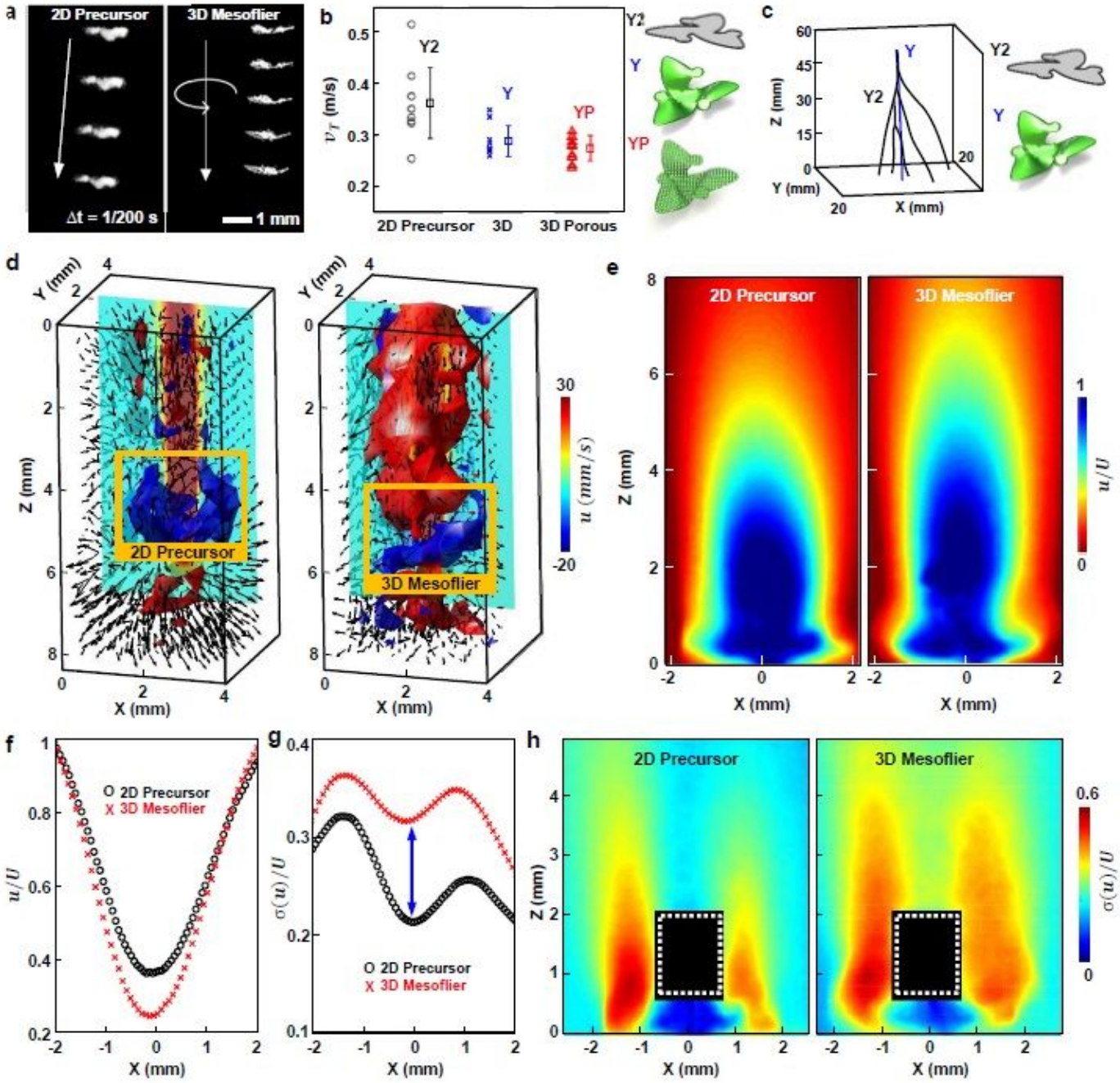

Figure 3

Experimental measurements of the flow characteristics of representative 3D mesofliers. a, Optical images of Y2 = a 2D precursor for a 3D mesoflier [3,M,0.4] and a corresponding 3D mesoflier Y = [3,M,0.4] at various times during free fall. The former shows nonrotating and random tumbling behaviors; the latter exhibits strong rotational dynamics and a straight path trajectory. b, Mean terminal velocity and its standard deviation for Y2 = a 2D precursor for a 3D mesoflier [3,M,0.4] and 3D mesoflier Y = [3,M,0.4], and YP = a porous 3D mesoflier for [3,PM,0.4]. c, Falling trajectories upon release at an angle of 900, where 00 corresponds to the flat side parallel to the ground. Y2 = a 2D precursor for a 3D mesoflier [3,M,0.4] and 3D mesoflier Y = [3,M,0.4]. d, Instantaneous 3D flow velocity fields induced by a free-falling 2D precursor for a 3D mesoflier [3,M,0.4] (left) and a 3D mesoflier [3,M,0.4] (right) determined via 3D-PTV. Red and blue iso-surfaces indicate iso-values of 15 and -5 mm/s, respectively. The color denotes correlated CFD results of the in-plane 2D vertical velocity along the center plane of the flier. PIV measurements of instantaneous flow fields induced by a physically constrained a 2D precursor for a 3D mesoflier [3,M,0.4] and a 3D mesoflier [3,M,0.4] in a wind tunnel. e, Mean velocity fields of a 2D precursor for a 3D mesoflier [3,M,0.4] (left) and a 3D mesoflier [3,M,0.4] (right) in these conditions, with a wind velocity U≈0.4 m/s. f, g, Velocity profiles (f) and vertical velocity fluctuation profiles (g) at x=4 mm downstream. h, Vertical velocity fluctuation σ(u) for a 2D precursor for a 3D mesoflier [3,M,0.4] (left) and a 3D mesoflier [3,M,0.4] (right).

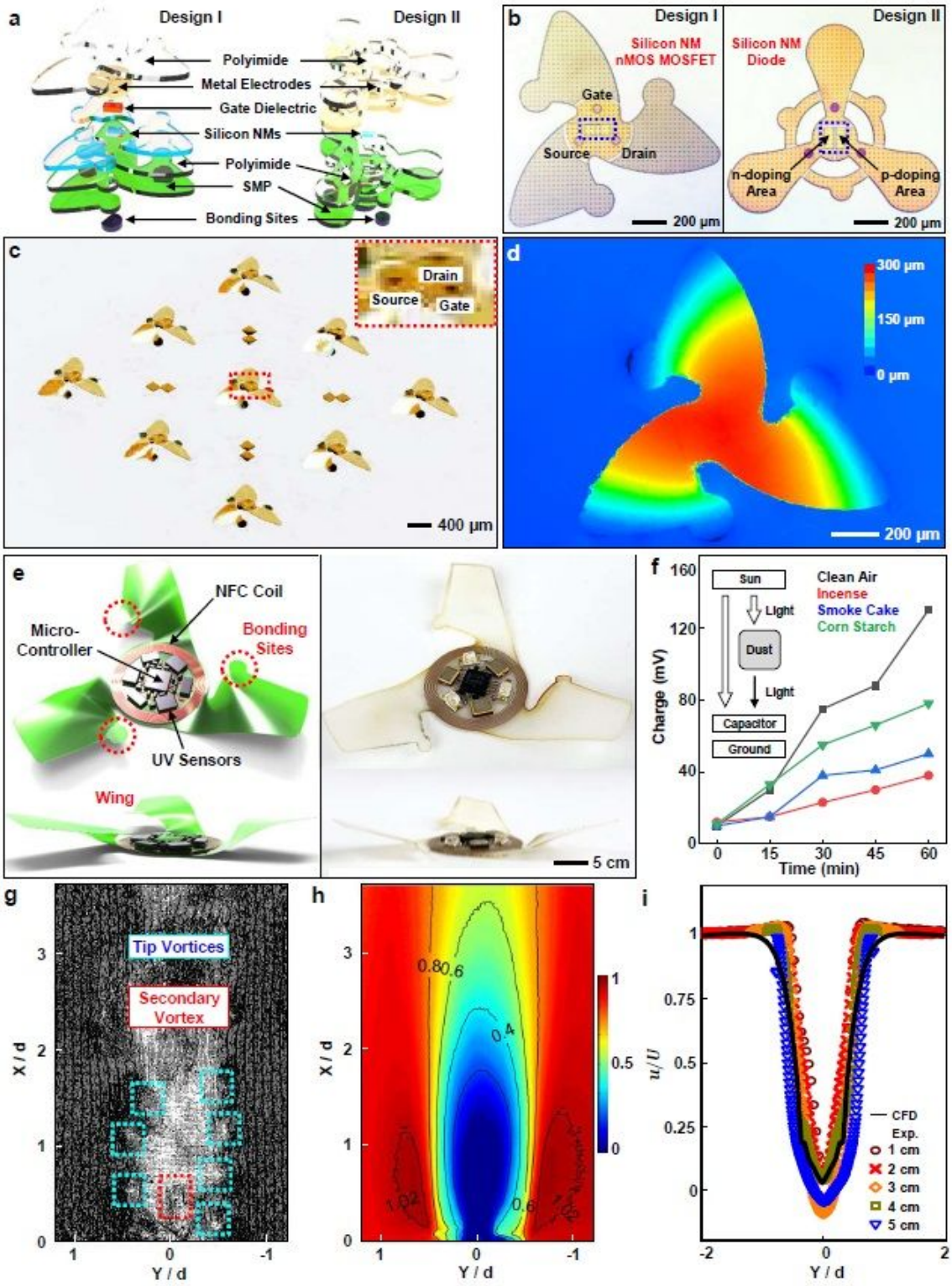

Figure 4

3D electronic mesofliers and IoT macrofliers. a,b, Schematic illustration (a) and optical micrographs (b) of 2D precursors for 3D electronic mesofliers [3,M,0.4] and [3,H,0.75] with silicon nanomembrane (NM) nMOS transistors and diodes as payloads. c, Photograph of a 3 x 3 array of 3D electronic mesofliers [3, M, 0.4] with these payloads. d, 3D surface profile of a 3D mesoflier [3,M,0.4]. e, Mechanical simulation results and photograph of a 3D IoT macroflier with a circuit to measure fine dust pollution through the

light dosimetry method. f, Energy stored on the SC as a function of exposure time in the presence of 3 types of fine dust. High-speed PIV flow measurements for 3D IoT macrofliers (d=2 cm) with various diameters and air velocities. g, Instantaneous velocity field. h, Mean velocity field u⁄U. i, Normalized spanwise velocity profiles at 1.2 diameter downstream for 3D IoT macrofliers with diameters between 1 and 5 cm.

Supplementary Files

This is a list of supplementary files associated with this preprint. Click to download.

- MFSI.pdf
- MFSN.docx
- MFSV1.mp4
- MFSV2.mp4
- MFSV3.mp4
- MFSV4.mp4
- MFSV5.mp4
- MFSV6.mp4
- MFSV7.mp4